PROCEEDINGS A

rspa.royalsocietypublishing.org

Research

Article submitted to journal

Subject Areas:
civil engineering

Keywords:
air-water flows, Froude scaling laws, Lie groups, scale effects, self-similarity

Author for correspondence:
Daniele Catucci
e-mail: daniele.catucci@nottingham.ac.uk

Numerical validation of novel scaling laws for air entrainment in water

Daniele Catucci[1], Riccardo Briganti[1] and Valentin Heller[1]

[1]Environmental Fluid Mechanics and Geoprocesses Research Group, Department of Civil Engineering, University of Nottingham, Nottingham NG7 2RD, UK

The Froude scaling laws have been common to model a wide range of water flows at reduced size for almost one century. In such Froude scale models, significant scale effects for air-water flows (e.g. hydraulic jumps or wave breaking) are typically observed. This study introduces novel scaling laws, excluding scale effects in the modelling of air-water flows. This is achieved by deriving the conditions under which the governing equations are self-similar. The one parameter Lie group of point scaling transformations is applied to the Reynolds-averaged Navier-Stokes equations, including surface tension effects. The scaling relationships between variables are derived for the flow variables, fluid properties and initial and boundary conditions. Numerical simulations are conducted to validate the novel scaling laws for (i) a dam break flow interacting with an obstacle and (ii) a vertical plunging water jet. Results for flow variables, void fraction and turbulent kinetic energy are shown to be self-similar at different scales, i.e. they collapse in dimensionless form. Moreover, these results are compared with those obtained using the traditional Froude scaling laws showing significant scale effects. The novel scaling laws are a more universal and flexible alternative with a genuine potential to improve laboratory modelling of air-water flows.

1. Introduction

Physical modelling at reduced size is one of the oldest and most important design tools in hydraulic engineering. For processes of engineering interest involving free surface flows, the Froude scaling laws have been used since they were introduced by Moritz Weber in 1930 [1]. They ensure that the ratio between the

THE ROYAL SOCIETY
PUBLISHING

inertial and gravity force, namely the Froude number Fr, is the same in the model and in nature, i.e. in the prototype. Other force ratios, such as the Reynolds number Re (inertial force to viscous force) and the Weber number We (inertial force to surface tension force), are represented incorrectly if the fluid properties are the same in the prototype and its model [2–4]. Froude scaling laws are particularly useful for laminar flows (Re $\rightarrow 0$) and also for fully turbulent flows (Re $\rightarrow \infty$) to investigate Reynolds number invariant fluid parameters [5,6].

However, the Froude scaling laws are also used for flows involving air-entrainment, e.g. air bubbles entrapment into water flows, hereafter referred to as air-water flows. For these, density, viscosity and surface tension between water and air play a central role such that Fr, Re and We are all important [7,8]. Indeed, most studies suggest that the Froude scaling laws without scaled fluid properties underestimate air entrainment because the effects of viscosity and surface tension are over-represented in the model [9–11].

Air-water flows are observed in many hydraulic phenomena such as spillway flows, hydraulic jumps, wave breaking and plunging jets, which are still modelled with Froude scaling laws, despite of their limitations [12–14]. Moreover, air-entrainment occurs at the free surface of oceans, rivers and streams as an important mechanism for the transport of oxygen and carbon dioxide, critical for the survival of these ecosystems [15,16]. Despite of many studies, turbulent air-water flows remain not well understood such that costly case-specific, large-scale investigations are commonly required to avoid scale effects [2].

An analytical approach to derive novel scaling laws can be based upon self-similarity of the governing equations. A self-similar object is identical to a part of itself. As such, the scaling of an object that follows suitable laws results in a self-similar scaled copy of the object itself [17–20] and a self-similar process behaves the same way at different scales, such that scale effects are avoided [21]. For example, a scaled model and the prototype of a hydraulic jump are self-similar if dimensionless results are identical. This implies that the dimensionless velocity field and the void fraction are variables that are invariant when self-similarity is achieved.

Self-similar conditions for phenomena with negligible surface tension effects have previously been derived by applying the one-parameter Lie group of point scaling transformations [22] (hereafter referred to as Lie group transformations). Lie group transformations are originally used to reduce the number of independent variables of an initial-boundary value problem by transforming it in a new space where the solution of the problem is the same as the original [20,23,24]. This approach has been applied by [25] to derive the conditions under which various hydrological processes are self-similar through the change in size. Consequently, the Lie group transformations can be used to find the scaling laws of the variables that can guarantee self-similarity of a phenomenon. The advantage of this approach is that it gives a complete picture of the requirements that must be satisfied for self-similarity, in contrast with a classical dimensional analysis, based on Buckingham π theorem, which is only applied to the dynamics in the interior of the domain and not to the boundary conditions [26,27].

Self-similar conditions of a depth-averaged 2D hydrodynamic equations system and the 3D Reynolds-Averaged Navier-Stokes (RANS) equations were derived in [28,29]. These two showed self-similar conditions of the variables in the RANS equations with k-ϵ closure for phenomena that are dominated by gravity and viscous effects. The scaling laws found by [29] were applied numerically to a lid-driven cavity flow, showing self-similar behaviour. In both studies [28] and [29], Computational Fluid Dynamics (CFD) was used to demonstrate that the proposed scaling laws involve no scale effects. Indeed, CFD can be used to investigate scale effects numerically and the scale and properties of fluids are more easily controlled than in laboratory experiments [30–33].

To the knowledge of the authors, there are no studies addressing the analytical conditions for which the governing equations involving viscous and surface tension effects are simultaneously self-similar when scaled in size. In the present study, we derive novel scaling laws by applying the Lie group transformations to the governing equations of air-water flows including surface tension effects. No other assumptions are made in the application of the Lie group transformations. This article shows, by simulating a range of scales, that the derived self-similar conditions for air-water flows and their boundary conditions can be used to achieve self-similarity.

The derived scaling laws are applied numerically to two air-water flow processes, namely (i) a dam break flow interacting with an obstacle, generating large deformations of the free surface [34], and (ii) a vertical circular plunging water jet impinging on quiescent water characterised by significant air entrainment, based on the experimental results of [13]. The 3D RANS equations govern both phenomena in which both viscosity and surface tension play a central role.

Air-water flows are here simulated by using *interFoam*, a numerical solver for 2-phase incompressible fluids flows based on the Volume of Fluid (VOF) method implemented in the OpenFOAM v1706 CFD package [35]. In these simulations, all the boundary and initial conditions, including the properties of the fluid, are transformed using the novel scaling laws at different geometrical scales with scale factors $\lambda = \frac{l_p}{l_m}$, where l_p is a characteristic length in the prototype (subscript p) and l_m the corresponding one in the model (subscript m). The processes are scaled using values of λ for which a correct representation of surface tension and viscous effects are essential to avoid significant scale effects. The two processes are also simulated with the commonly applied Froude scaling laws using ordinary water and air in the model, as common in laboratory experiments (herein called *traditional Froude scaling*), and the Froude scaling laws in which the properties of the fluids are strictly scaled (herein called *precise Froude scaling*). It is demonstrated that the novel scaling laws involve no scale effects, in contrast to traditional Froude scaling, and they are also more universal and flexible than precise Froude scaling.

This article is organised as follows: in Sec. 2 the Lie group transformations are applied to the governing equations and the novel scaling laws are derived. The numerical model is presented in Sec. 3. Subsequently, the two CFD case studies are illustrated in Sec. 4, including the set-up, the application of the novel scaling laws and the results. The findings of this research are discussed in Sec. 5 and the conclusions and recommendations for future work are given in Sec. 6. Finally, Appendix A includes the details of the derivation of the novel scaling laws and the self-similar conditions due to the initial and boundary conditions.

2. Analytical derivation of the novel scaling laws

(a) Governing equations

Air-water flows are here described by the RANS equations for incompressible fluids:

$$\frac{\partial U_{\mathrm{j}}}{\partial x_{\mathrm{j}}} = 0 \tag{2.1}$$

and

$$\frac{\partial U_{\mathrm{i}}}{\partial t} + U_{\mathrm{j}}\frac{\partial U_{\mathrm{i}}}{\partial x_{\mathrm{j}}} = \frac{\partial}{\partial x_{\mathrm{j}}}\left(\nu\frac{\partial U_{\mathrm{i}}}{\partial x_{\mathrm{j}}} - \overline{u_{\mathrm{i}}u_{\mathrm{j}}}\right) - \frac{1}{\rho}\frac{\partial p}{\partial x_{\mathrm{i}}} + g_{\mathrm{i}} + \frac{1}{\rho}f_{\sigma}, \quad \mathrm{i},\mathrm{j} = 1,2,3, \tag{2.2}$$

where i is the free index, j the dummy index, following Einstein's notation, t is time, x_{i} and x_{j} are the spatial coordinates, U_{i} and U_{j} the Reynolds-averaged flow velocity components, u_{i} and u_{j} the fluctuating velocity components, $\overline{u_{\mathrm{i}}u_{\mathrm{j}}}$ is the Reynolds stress term, p the Reynolds-averaged pressure, ν the kinematic viscosity, ρ the density of the fluid, $g_{\mathrm{i}} = (g_1, g_2, g_3)$ the gravitational acceleration vector and f_{σ} the surface tension force per unit volume defined as

$$f_{\sigma} = \sigma\kappa\frac{\partial \gamma}{\partial x_{\mathrm{i}}}. \tag{2.3}$$

In Eq. (2.3) σ is the surface tension constant, κ the curvature of the free surface and γ the phase fraction. This is a dimensionless variable with values between 0 and 1 that is used to identify any air/water interface (see Sec. 3). The k-ϵ model is here applied for the Reynolds-stresses in Eq. (2.2), (see [36] for more details), for which

$$-\overline{u_i u_j} = \nu_t \left(\frac{\partial U_i}{\partial x_j} + \frac{\partial U_j}{\partial x_i} \right) - 2/3 k \delta_{ij}, \tag{2.4}$$

where k is the turbulent kinetic energy, δ_{ij} the Kronecker delta and ν_t the eddy viscosity

$$\nu_t = C_\mu k^2/\epsilon. \tag{2.5}$$

k, and its rate of dissipation ϵ, are calculated from

$$\frac{\partial k}{\partial t} + U_j \frac{\partial k}{\partial x_j} = P_k - \epsilon + \frac{\partial}{\partial x_j}\left[(\nu + \nu_t / C_{\sigma_k}) \frac{\partial k}{\partial x_j} \right] \tag{2.6}$$

and

$$\frac{\partial \epsilon}{\partial t} + U_j \frac{\partial \epsilon}{\partial x_j} = C_{\epsilon 1} \frac{\epsilon}{k} P_k - C_{\epsilon 2} \frac{\epsilon^2}{k} + \frac{\partial}{\partial x_j}\left[(\nu + \nu_t / C_{\sigma_\epsilon}) \frac{\partial \epsilon}{\partial x_j} \right]. \tag{2.7}$$

$P_k = u_t \frac{\partial U_i}{\partial x_j} \left(\frac{\partial U_i}{\partial x_j} + \frac{\partial U_j}{\partial x_i} \right)$ and $C_{\epsilon 1} = 1.44$, $C_{\epsilon 2} = 1.92$, $C_\mu = 0.09$, $C_{\sigma_k} = 1.0$ and $C_{\sigma_\epsilon} = 1.3$ are the standard model coefficients used in the k-ϵ turbulence model [37]. The approach used her for turbulence modelling, combined with the VOF method has been recognised to overestimate k [38], although this does not affect the derivation of the scaling laws and the self-similarity of the representation of the process.

(b) One parameter Lie group transformations

The Lie group is defined as

$$\phi = \beta^{\alpha_\phi} \phi^*. \tag{2.8}$$

Eq. (2.8) transforms the variable ϕ in the original space into the variable ϕ^* in the transformed (*) space, β is the scaling parameter and α_ϕ the scaling exponent of the variable ϕ. The scaling ratio of the variable ϕ is $r_\phi = \phi/\phi^* = \beta^{\alpha_\phi}$ [29,39].

All the variables of Eqs. (2.1) to (2.7) in the original domain are written in the transformed domain as:

$$\begin{aligned}
x_1 = \beta^{\alpha_{x_1}} x_1^*, \quad x_2 = \beta^{\alpha_{x_2}} x_2^*, \quad x_3 = \beta^{\alpha_{x_3}} x_3^*, \quad t = \beta^{\alpha_t} t^*, \\
U_1 = \beta^{\alpha_{U_1}} U_1^*, \quad U_2 = \beta^{\alpha_{U_2}} U_2^*, \quad U_3 = \beta^{\alpha_{U_3}} U_3^*, \quad p = \beta^{\alpha_p} p^*, \\
g_i = \beta^{\alpha_g} g_i^*, \quad \rho = \beta^{\alpha_\rho} \rho^*, \quad \nu = \beta^{\alpha_\nu} \nu^*, \quad \sigma = \beta^{\alpha_\sigma} \sigma^*, \quad \kappa = \beta^{\alpha_\kappa} \kappa^*, \\
u_1 = \beta^{\alpha_{u_1}} u_1^*, \quad u_2 = \beta^{\alpha_{u_2}} u_2^*, \quad u_3 = \beta^{\alpha_{u_3}} u_3^*, \\
k = \beta^{\alpha_k} k^*, \quad \epsilon = \beta^{\alpha_\epsilon} \epsilon^*, \quad \nu_t = \beta^{\alpha_{\nu_t}} \nu_t^*, \quad P_k = \beta^{\alpha_{P_k}} P_k^*.
\end{aligned} \tag{2.9}$$

Self-similar conditions are obtained when the governing equations in the original domain, subjected to the Lie group transformations, remain invariant. The Lie group transformations for Eq. (2.1) yields the following equation in the transformed domain

$$\frac{\partial \beta^{\alpha_{U_1}} U_1^*}{\partial \beta^{\alpha_{x_1}} x_1^*} + \frac{\partial \beta^{\alpha_{U_2}} U_2^*}{\partial \beta^{\alpha_{x_2}} x_2^*} + \frac{\partial \beta^{\alpha_{U_3}} U_3^*}{\partial \beta^{\alpha_{x_3}} x_3^*} = 0, \tag{2.10}$$

which, with β being a constant parameter, is rearranged as

$$\beta^{\alpha_{U_1}-\alpha_{x_1}}\frac{\partial U_1^*}{\partial x_1^*}+\beta^{\alpha_{U_2}-\alpha_{x_2}}\frac{\partial U_2^*}{\partial x_2^*}+\beta^{\alpha_{U_3}-\alpha_{x_3}}\frac{\partial U_3^*}{\partial x_3^*}=0. \tag{2.11}$$

Self-similarity is achieved if Eq. (2.11) can be obtained from Eq. (2.1) by means of a simple scaling process. Therefore, all terms of Eq. (2.11) must be transformed by using the same scaling ratios:

$$\beta^{\alpha_{U_1}-\alpha_{x_1}}=\beta^{\alpha_{U_2}-\alpha_{x_2}}=\beta^{\alpha_{U_3}-\alpha_{x_3}} \quad\Rightarrow\quad \alpha_{U_1}-\alpha_{x_1}=\alpha_{U_2}-\alpha_{x_2}=\alpha_{U_3}-\alpha_{x_3}. \tag{2.12}$$

Table 1. Novel and precise Froude scaling laws for the variables of the RANS equations and the k-ϵ turbulence model obtained by applying the Lie group transformations.

Variables	Scaling conditions in terms of α_x, α_t and α_ρ (novel scaling laws)		Scaling conditions in terms of α_x, α_ρ and $\alpha_g=0$		Scaling conditions in terms of α_x, $\alpha_\rho=\alpha_g=0$ (precise Froude scaling laws)	
	Exponents	Scaling ratios	Exponents	Scaling ratios	Exponents	Scaling ratios
Length (m)	α_x	β^{α_x}	α_x	β^{α_x}	α_x	$\beta^{\alpha_x}=\lambda$
Time (s)	α_t	β^{α_t}	$\alpha_t=0.5\alpha_x$	$\beta^{0.5\alpha_x}$	$\alpha_t=0.5\alpha_x$	$\beta^{0.5\alpha_x}=\lambda^{0.5}$
Density (kg/m^3)	α_ρ	β^{α_ρ}	α_ρ	β^{α_ρ}	$\alpha_\rho=0$	$\beta^0=1$
Velocity (m/s)	$\alpha_U=\alpha_x-\alpha_t$	$\beta^{\alpha_x-\alpha_t}$	$\alpha_U=0.5\alpha_x$	$\beta^{0.5\alpha_x}$	$\alpha_U=0.5\alpha_x$	$\beta^{0.5\alpha_x}=\lambda^{0.5}$
Pressure (Pa)	$\alpha_p=2\alpha_x-2\alpha_t+\alpha_\rho$	$\beta^{2\alpha_x-2\alpha_t+\alpha_\rho}$	$\alpha_p=\alpha_x+\alpha_\rho$	$\beta^{\alpha_x+\alpha_\rho}$	$\alpha_p=\alpha_x$	$\beta^{\alpha_x}=\lambda$
Gravitational acceleration (m/s^2)	$\alpha_g=\alpha_x-2\alpha_t$	$\beta^{\alpha_x-2\alpha_t}$	$\alpha_g=0$	$\beta^0=1$	$\alpha_g=0$	$\beta^0=1$
Viscosity (m^2/s)	$\alpha_\nu=2\alpha_x-\alpha_t$	$\beta^{2\alpha_x-\alpha_t}$	$\alpha_\nu=1.5\alpha_x$	$\beta^{1.5\alpha_x}$	$\alpha_\nu=1.5\alpha_x$	$\beta^{1.5\alpha_x}=\lambda^{1.5}$
Surface tension (N/m)	$\alpha_\sigma=3\alpha_x-2\alpha_t+\alpha_\rho$	$\beta^{3\alpha_x-2\alpha_t+\alpha_\rho}$	$\alpha_\sigma=2\alpha_x+\alpha_\rho$	$\beta^{2\alpha_x+\alpha_\rho}$	$\alpha_\sigma=2\alpha_x$	$\beta^{2\alpha_x}=\lambda^2$
Curvature of the free surface (1/m)	$\alpha_\kappa=\alpha_x^{-1}$	$\beta^{\alpha_x^{-1}}$	$\alpha_\kappa=\alpha_x^{-1}$	$\beta^{\alpha_x^{-1}}$	$\alpha_\kappa=\alpha_x^{-1}$	$\beta^{\alpha^{-1}}=\lambda^{-1}$
Eddy viscosity (m^2/s)	$\alpha_{\nu_t}=2\alpha_x-\alpha_t$	$\beta^{2\alpha_x-\alpha_t}$	$\alpha_{\nu_t}=1.5\alpha_x$	$\beta^{1.5\alpha_x}$	$\alpha_{\nu_t}=1.5\alpha_x$	$\beta^{1.5\alpha_x}=\lambda^{1.5}$
Reynolds stresses (m^2/s^2)	$\alpha_{\langle u_i,u_j\rangle}=2\alpha_x-2\alpha_t$	$\beta^{2\alpha_x-2\alpha_t}$	$\alpha_{\langle u_i,u_j\rangle}=\alpha_x$	β^{α_x}	$\alpha_{\langle u_i,u_j\rangle}=\alpha_x$	$\beta^{\alpha_x}=\lambda$
Turbulent kinetic energy (m^2/s^2)	$\alpha_k=2\alpha_x-2\alpha_t$	$\beta^{2\alpha_x-2\alpha_t}$	$\alpha_k=\alpha_x$	β^{α_x}	$\alpha_k=\alpha_x$	$\beta^{\alpha_x}=\lambda$
Dissipation (m^2/s^3)	$\alpha_\epsilon=2\alpha_x-3\alpha_t$	$\beta^{2\alpha_x-3\alpha_t}$	$\alpha_\epsilon=0.5\alpha_x$	$\beta^{0.5\alpha_x}$	$\alpha_\epsilon=0.5\alpha_x$	$\beta^{0.5\alpha_x}=\lambda^{0.5}$
Production of turbulence due to horizontal velocity gradients (m^2/s^3)	$\alpha_{P_k}=2\alpha_x-3\alpha_t$	$\beta^{2\alpha_x-3\alpha_t}$	$\alpha_{P_k}=0.5\alpha_x$	$\beta^{0.5\alpha_x}$	$\alpha_{P_k}=0.5\alpha_x$	$\beta^{0.5\alpha_x}=\lambda^{0.5}$

To attain self-similarity of air-water flows, the exponents for length, velocity and fluctuating velocity components have to be identical for the i^{th} axis. This is shown in Appendix A where the detailed derivation of Eqs. (2.2) to (2.7) is presented. Hereafter, α_x, α_U and α_u are used to indicate the scaling exponents of length, Reynolds-averaged velocity and fluctuating velocity components on the i^{th} axis. Similarly, α_ρ, α_ν and α_σ are derived by applying the Lie group transformations to Eq. (2.3). Further, based on Eqs. (2.5) to (2.7), the scaling conditions for the turbulent parameters are derived. In addition, the detailed derivation of the self-similar conditions for the initial and boundary conditions are also shown in Appendix A. The scaling conditions derived above are summarised in the second column of Table 1. They are consistent with those reported in Table 1 and 2 in [29] with addition of the surface tension and the curvature of the free surface. All the exponents are written in terms of three independent scaling exponents, namely α_x, α_t and α_ρ, meaning that they are user-defined (their choice is flexible). In fact, the solution of air-water flows equations can be mapped to solutions in other transformed domains with different $\lambda=\beta^{\alpha_x}$ by selecting the scaling parameter β and changing the α of three independent variables.

It is possible to assign the value of one or two of the three α while still preserving self-similarity. For example, in Table 1 it is shown that choosing $\alpha_g=0$ implies that $\alpha_g=\alpha_x-2\alpha_t$. Therefore, the unscaled g requires that $\alpha_t=0.5\alpha_x$. In this configuration, the remaining scaling exponents are written in terms of α_x, α_ρ and $\alpha_g=0$ (fourth and fifth columns of Table 1). Hence, keeping g invariant in a scaled model requires to scale time and flow velocities and to change the properties of the fluids to obtain a self-similar behaviour. A further restriction can be imposed on the density of the fluids, namely $\alpha_\rho=0$. This restriction leads to the well-known precise Froude scaling laws [3], as a particular case of the novel scaling laws, where g is constant and ν and ρ are scaled by keeping Re and We invariant.

3. Numerical model

Air-water flows are simulated by using the 2-phases flow solver *interFoam*, based on the VOF method, implemented in the OpenFOAM v1706 CFD package [35]. A single system of RANS equations is solved with the pressure and velocity fields shared among both phases. The interface between water and air is identified by a value of the phase fraction γ between $\gamma = 1$ (water) and $\gamma = 0$ (air). The fluid properties used in the equations are mapped in all domains as a weighted average using γ as weight, e.g. for ρ and ν:

$$\rho = \gamma\rho_w + (1-\gamma)\rho_a, \tag{3.1}$$

$$\nu = \gamma\nu_w + (1-\gamma)\nu_a, \tag{3.2}$$

where subscripts w and a refer to the water and air phase, respectively. σ appears in Eq. (2.3) to model the surface tension force per unit volume, as stated in the Continuum Surface Force method proposed by [40]. The curvature of the interface between two fluids κ is defined as

$$\kappa = -\frac{\partial}{\partial x_\mathrm{i}}\left(\frac{\partial\gamma/\partial x_\mathrm{i}}{\mid \partial\gamma/\partial x_\mathrm{i}\mid}\right). \tag{3.3}$$

γ is transported as a scalar by the flow field and the interface location (e.g. the free surface) is updated by solving the volume fraction equation

$$\frac{\partial\gamma}{\partial t} + \frac{\partial(\gamma U_\mathrm{j})}{\partial x_\mathrm{j}} = 0. \tag{3.4}$$

The interface reconstruction technique used by *interFoam* is MULES [41]. The free surface can also be captured by using alternative techniques, such as the *isoAdvector* method [42]. However, the governing equations remain the same and the self-similarity of the representation of the process under the novel scaling laws is not affected by the interface reconstruction technique.

4. Numerical results

The self-similar conditions of the novel scaling laws are validated with the simulation of two physical processes: (i) a dam break flow interacting with an obstacle and (ii) a vertical plunging water jet. The simulations for both processes involve the prototype and a number of scaled models up to large geometrical scale factors of $\lambda = 16$.

(a) Dam break flow

Dam break flows have been widely investigated numerically and the specific case addressed herein is chosen because it is a well-known test to validate the modelling of large deformations of free surfaces [43,44]. The solver used in the present study has been validated with this particular test case by [34]. In this study, $\gamma = 0.1$ is selected to identify the air/water interface in the VOF method. $\gamma = 0.1$ is obtained by considering the value between 0 and 1 providing the best fit with the experimental void fraction distribution in Sec. 4(b).

(i) Numerical set-up

The initial condition at $t = 0$ consists of a quiescent water column of volume $1.228 \times 0.550 \times 1.000$ m^3, located at the left side of a $3.220 \times 1.000 \times 1.000$ m^3 tank (Fig. 1). A prismatic fixed obstacle with a volume of $0.160 \times 0.160 \times 0.403$ m^3 is located at $x_1 = 2.395$ m. The water column is released instantaneously at $t = 0$. Subsequently, the flow impacts the obstacle and creates a complex two-phase flow. The top wall of the domain is modelled as an open, fully transmissive boundary at atmospheric pressure and all the remaining walls as no-slip boundary conditions. The water density is $\rho_w = 1000$ kg/m^3, its kinematic viscosity $\nu_w = 1 \times 10^{-6}$ m^2/s and the surface tension constant $\sigma = 0.07$ N/m.

A 180 (length) × 60 (width) × 80 (height) Cartesian computational grid was used, apart from the obstacle. Note that, due to the orientation of the reference frame, for this case $g_{\rm i} = (0, 0, -g)$ in Eq. (2.2). The time step Δt was set equal to 0.001 s at the start of the simulation and it was varied subsequently by respecting the CFL condition

$$\frac{U_{\rm j}\Delta t}{\Delta x_{\rm j}} < C_{max}, \tag{4.1}$$

where $\Delta x_{\rm i}$ is the mesh size in the Cartesian coordinate system and $C_{max} = 0.8$ the maximum Courant number following [45]. The simulations were run on the University of Nottingham High Performance Computing (HPC) cluster Augusta. The number of cells in the computational domain was 861075 and the used cores and memory were 4 and 36 GB, respectively. It required 2 h to simulate the real time of 6 s (also for the corresponding times at reduced scales). In this test case, as well as for the jet, all the dimensional parameters, including the mesh sizes and time steps, were scaled to the smaller domains according to the selected scaling laws.

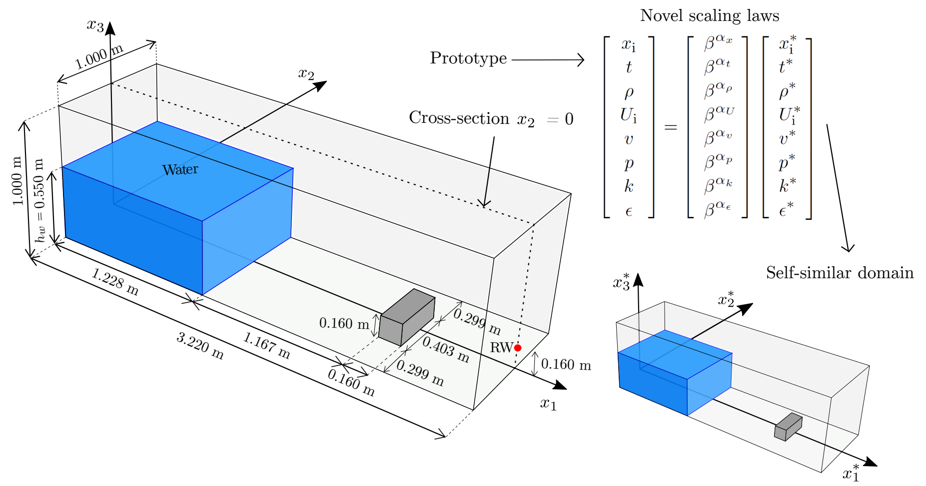

Figure 1. Initial set-up of the dam break flow prototype and a scaled numerical domain to schematically illustrate the novel scaling laws. The flow parameters at a specified time and space can be transformed to the corresponding time and space in the self-similar domain.

(ii) Application of the novel scaling laws

Two self-similar domains, namely D8 and D16, are created with geometrical scale factors of $\lambda = \beta^{\alpha_x} = 8$ and 16, respectively. To achieve this, it is assumed that $\alpha_x = 1$ such that $\beta = 8$ (D8) and 16 (D16), respectively. All variables and parameters are transformed by the scaling exponents in the fourth and fifth columns of Table 2 (with scaling conditions in terms of α_x, α_t and $\alpha_g = 0$). Their specific values for the prototype and the scaled models, obtained by applying the conditions in Table 2, are presented in Table 3. The prototype is also scaled by using precise Froude scaling (D8$_{\rm PFr}$ and D16$_{\rm PFr}$) and traditional Froude scaling (D8$_{\rm TFr}$ and D16$_{\rm TFr}$) using the same λ as in the self-similar domains.

Table 2. Scaling parameters and exponents used to scale the dam break flow prototype values to the corresponding values in the domains D8 and D16 using the novel scaling laws.

	Domain D8	Domain D16
Scaling parameter β	8	16
Scaling exponents		
Length (m) α_x	1	
Time (s) α_t	0.5	
Density (kg/m^3) α_ρ	1	
Velocity (m/s) α_U	0.5	
Pressure (Pa) α_p	2	
Viscosity (m^2/s) α_ν	1.5	
Surface tension (N/m) α_σ	3	
Scaling ratios		
Length (m) β^{α_x}	8	16
Time (s) β^{α_t}	2.82	4
Density (kg/m^3) β^{α_ρ}	8	16
Velocity (m/s) β^{α_U}	2.82	4
Pressure (Pa) β^{α_p}	64	256
Viscosity (m^2/s) β^{α_ν}	22.62	64
Surface tension (N/m) β^{α_σ}	512	4096

Table 3. Parameters for the dam break flow in the prototype and the scaled domains.

Variables	Prototype D1	Domain D8	Domain D16	Domain D8$_{\mathrm{PFr}}$	Domain D16$_{\mathrm{PFr}}$	Domain D8$_{\mathrm{TFr}}$	Domain D16$_{\mathrm{TFr}}$
Tank length (m)	3.22	0.4025	0.20125	0.4025	0.20125	0.4025	0.20125
Water column height (m)	0.55	0.06875	0.034375	0.06875	0.034375	0.06875	0.034375
Computational time (s)	6	2.12	1.5	2.12	1.5	2.12	1.5
Gravitational acceleration (m/s^2)	9.81	9.81		9.81		9.81	
Water density (kg/m^3)	1000	125	62.5	1000		1000	
Water viscosity (m^2/s)	10^{-6}	4.42×10^{-8}	1.56×10^{-8}	4.42×10^{-8}	1.56×10^{-8}	10^{-6}	
Air density (kg/m^3)	1	0.125	0.0625	1		1	
Air viscosity (m^2/s)	1.48×10^{-5}	6.54×10^{-7}	2.31×10^{-7}	6.54×10^{-7}	2.31×10^{-7}	1.48×10^{-5}	
Surface tension (N/m)	0.07	1.37×10^{-4}	1.70×10^{-5}	1.09×10^{-3}	2.73×10^{-4}	0.07	

(iii) Results

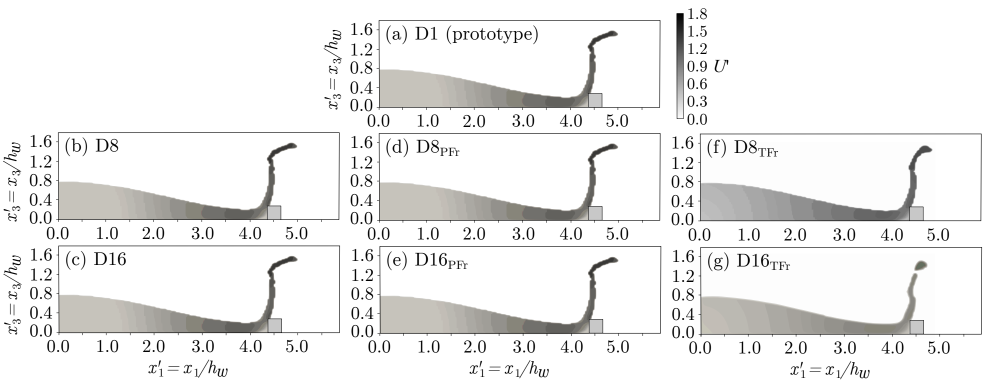

Figure 2. Snapshots of the dam break flow at the cross-section $x'_2 = 0$ and dimensionless time $t' = 2.7$ of the (a) prototype and scaled with (b,c) the novel scaling laws, (d,e) precise Froude scaling and (f,g) traditional Froude scaling.

For the purpose of this work it is interesting to analyse the time when gravity, inertial, viscous and surface tension effects are all relevant. This happens when the dam break flow impacts the obstacle and creates an elongated water tongue. Fig. 2 shows this process with snapshots of the prototype and the scaled domains at $x'_2 = x_2/h_w = 0$ (Fig. 1) and dimensionless time $t' = t\sqrt{g/h_w} = 2.7$. The contours in Fig. 2 represent the dimensionless velocity magnitude $U' = U/\sqrt{gh_w}$, where $U = \sqrt{U_1^2 + U_2^2 + U_3^2}$. The prototype shows a large free surface deformation after impacting the obstacle (Fig. 2a). The self-similar domains and the domains scaled with precise Froude scaling all simulate the water tongue of the prototype correctly. Moreover, the dimensionless velocity magnitude in the prototype and in the self-similar domains are the same, despite of the increasing λ (Fig. 2b,c,d,e). On the other hand, traditional Froude scaling does not model the free surface correctly due to Re and We scale effects, i.e. the water tongue becomes less prolonged with increasing λ (Fig. 2f,g).

The differences between the prototype and the scaled domains are quantified using the Root Mean Square Error along the plane $x_2' = 0$ for U' (RMSE$_{U'}$)

$$\mathrm{RMSE}_{U'} = \sqrt{\frac{\sum_{\mathrm{b}=1}^{\mathrm{n}} (U'_{\mathrm{b},p} - U'_{\mathrm{b},m})^2}{\mathrm{n}}}, \tag{4.2}$$

where $U'_{\mathrm{b},p}$ are the cell values of U' in the prototype, $U'_{\mathrm{b},m}$ in the scaled domains and $\mathrm{n} = 14283$ is the number of cells in the cross-section $x_2' = 0$. As shown in Table 4, the RMSE$_{U'}$ values for D8 and D16 confirm a nearly perfect self-similarity with respect to the prototype.

Table 4. RMSE$_{U'}$ for the dam break flow for the domains D1 and D8, D16, D8$_{\mathrm{PFr}}$, D16$_{\mathrm{PFr}}$, D8$_{\mathrm{TFr}}$ and D16$_{\mathrm{TFr}}$, for the snapshots in Fig. 2.

RMSE$_{U'}$					
D1-D8	D1-D16	D1-D8$_{\mathrm{PFr}}$	D1-D16$_{\mathrm{PFr}}$	D1-D8$_{\mathrm{TFr}}$	D1-D16$_{\mathrm{TFr}}$
2.98×10^{-4}	2.10×10^{-4}	3.00×10^{-4}	2.21×10^{-4}	0.067	0.119

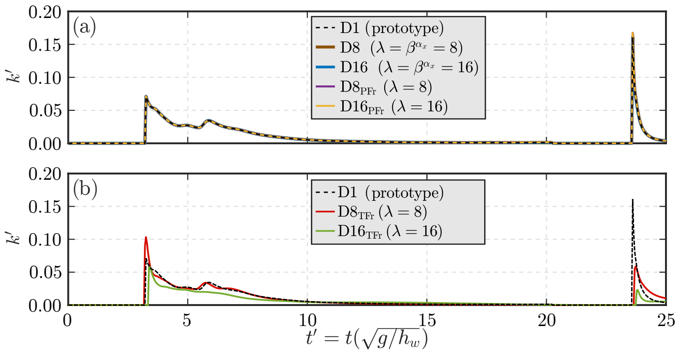

Figure 3. k' time histories in the dam break flow at point RW for (a) domains D1, D8, D16, D8$_{\mathrm{PFr}}$ and D16$_{\mathrm{PFr}}$ and (b) D1, D8$_{\mathrm{TFr}}$ and D16$_{\mathrm{TFr}}$.

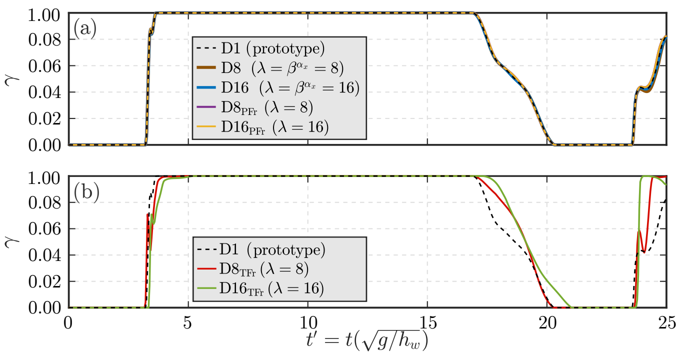

Figure 4. γ time histories in the dam break flow at point RW for (a) domains D1, D8, D16, D8$_{\mathrm{PFr}}$ and D16$_{\mathrm{PFr}}$ and (b) D1, D8$_{\mathrm{TFr}}$ and D16$_{\mathrm{TFr}}$.

k is used to assess turbulence because it shows significant scale effects if ν is not scaled. Air entrainment is assessed by using γ, which is expected to deviate from the prototype if the surface tension is over-represented in the scaled domain. Fig. 3 shows the dimensionless turbulent kinetic energy $k' = k/(gh_w)$ at point RW (Fig. 1) versus t' and the variation of γ is shown in Fig. 4. After $t' = 2.7$, the water tongue collapses and creates a complex flow characterised by strong turbulence and air entrainment. The flow reaches the downstream wall where it is reflected at $t' = 3.25$. At a later stage, the dam-break wave is re-reflected at the upstream wall and it reaches point RW again at $t' = 23.6$.

The perfect collapse of the data for D1, D8 and D16 affirms the self-similar behaviour of k' for the novel scaling laws. The self-similar behaviour is also confirmed for D8_{PFr} and D16_{PFr}. On the other hand, k' shows scale effects using traditional Froude scaling; the first k' peak is either under- or over-estimated (D8_{TFr} and D16_{TFr}, respectively), while the magnitude of the second peak decreases with increasing λ.

As demonstrated in Fig. 4, where γ is shown as a proxy for surface tension, air entrainment is correctly scaled in the self-similar domains as it controls the air-water interface and the free surface curvature. While the results in the domains D1, D8, D16, D8_{PFr} and D16_{PFr} essentially collapse, the domains scaled with traditional Froude scaling show significant differences in the region where air entrainment is most important. γ starts to increase close to $t' = 4$, meaning that the wave reaches RW consistently at the same time in all domains except for D8_{TFr} and D16_{TFr} (Fig. 4). Subsequently, γ increases to reach 1 less rapidly than in the prototype when using traditional Froude scaling. These differences become more visible at a later stage of the simulation when the dam break wave is re-reflected at $t' = 23.6$, showing significant scale effects.

(b) Plunging water jet

In this section, the same scaling laws as in the previous test case are applied to the plunging water jet presented in [13]. This involves free-surface instabilities, air entrainment and turbulence.

(i) Numerical setup

The setup is based on the experiments of [13], consisting of a jet from a circular orifice impinging on a prismatic column of water. However, in this study, the symmetry of the problem with respect to two orthogonal vertical planes is used to simulate only a quarter of the domain, in order to reduce the computational cost. Fig. 5 shows the numerical domain and the variables used in the prototype. A plunging water jet is ejected from a nozzle having a radius $r_{in} = 0.0125$ m. Here, the subscript in indicates the quantities at the nozzle, i.e. at the inlet of the numerical domain, while the subscript im indicates values of variables at the still water level, i.e. $x_1 = 0$. The receiving pool is 0.15 m wide and 1.80 m deep and at the start of the simulation the distance between the water surface and the nozzle is $l_1 = 0.10$ m. The velocity of the jet at $x_1 = 0$ is $U_{im} = 4.10$ m/s. Here, a Cartesian coordinate system with x_1 pointing downwards is used, therefore, $g_{\text{i}} = (g, 0, 0)$.

The inlet boundary condition, namely the nozzle, is at the top boundary. The velocity at the inlet U_{in} and both k_{in} and ϵ_{in} are prescribed, while the outlet is located at the bottom boundary, having the same flow rate magnitude as the inlet.

U_{in} is calculated starting from the jet impact velocity using Bernoulli's theorem $U_{in} = \sqrt{U_{im}^2 - 2gl_1} = 3.85$ m/s. At the outlet (subscript out) $U_{out} = U_{in}$ and $r_{out} = r_{in}$. k_{in} and ϵ_{in} are calculated as

$$k_{in} = \frac{3}{2}(U_{in}I)^2 = 0.000471 \text{ m}^2/\text{s}^2, \tag{4.3}$$

$$\epsilon_{in} = C_\mu \frac{k_{in}^{3/2}}{l_t} = 0.00105 \text{ m}^2/\text{s}^3, \tag{4.4}$$

where $I = 0.46\%$ is the turbulent intensity following [13], and l_t the turbulent mixing length approximated with $l_t = 0.07r_{in}$. The part of the top boundary of the domain not occupied by the inlet was modelled as a fully transmissive open boundary at atmospheric pressure. Since only a quarter of the domain is simulated, a symmetry boundary condition is used at the symmetry boundary walls and no-slip conditions are applied at the remaining walls, including the bottom wall outside the outlet cells (Fig. 5).

A structured orthogonal mesh is used with a finer resolution for the area in which the water jet impacts the free surface down to a depth of 0.6 m. The smallest observed bubble size was 1 mm and the minimum cell size 0.625 mm to increase the interface sharpness around the bubbles [13,46]. This mesh resolution is not fine enough to resolve the smallest bubbles present in the flow. However, the main focus of this work is to show the relative differences in the results of the application of different scaling laws for air-water flows, rather than to perfectly resolve the dynamics of individual bubbles.

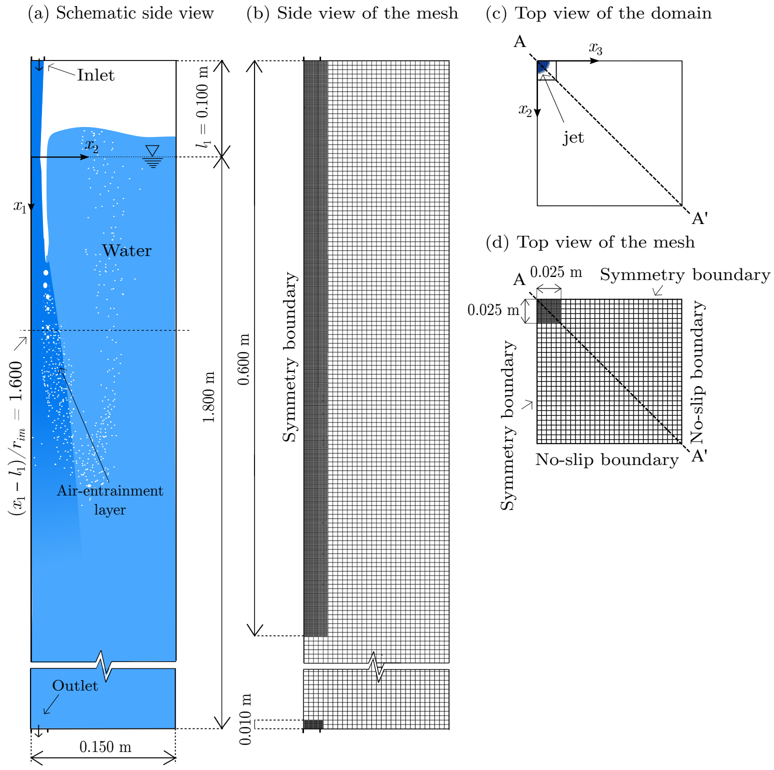

Figure 5. Schematic illustration of the computational domain and mesh of the plunging water jet.

The simulation time was 300 s, the same duration used by [13] to compute the distribution of the void fraction from the laboratory measurements, and the time step varied with respect to the CFL condition. C_{max} was set equal to 0.3. The simulations were run on the University of Nottingham HPC cluster Augusta. The number of cells in the computational domain was 1.89×10^6 and the corresponding cores and memory were 10 and 36 GB, respectively. It required 168 h to simulate 300 s real time (also for the corresponding times at reduced scales).

(ii) Application of the novel scaling laws

The two self-similar domains P8 and P16 were simulated with geometrical scale factors of $\lambda = 8$ and 16, respectively. Similarly to the dam break case, the scaling exponent for length is $\alpha_x = 1$ so that $\beta = 8$ (P8) and 16 (P16). The scaling ratios and parameters obtained by applying the conditions in the second column of Table 1 are shown in Table 5. The domains $\mathrm{P8_{PFr}}$ and $\mathrm{P16_{PFr}}$ refer to precise Froude scaling and $\mathrm{P8_{TFr}}$ and $\mathrm{P16_{TFr}}$ to traditional Froude scaling (Table 5).

Table 5. Scaling parameters and used exponents to scale the plunging jet prototype values to the corresponding values in the domains P8 and P16.

Variables	Prototype	Domain P8	Domain P16	Domain $P8_{PFr}$	Domain $P16_{PFr}$	Domain $P8_{TFr}$	Domain $P16_{TFr}$
Inlet radius (m)	0.0125	0.0015625	7.81×10^{-4}	0.0015625	7.81×10^{-4}	0.0015625	7.81×10^{-4}
Computational time (s)	300	106	75	106	75	106	75
Impact velocity (m/s)	4.10	1.45	1.025	1.45	1.025	1.45	1.025
Gravitational acceleration (m/s^2)	9.81	9.81		9.81		9.81	
Water density (kg/m^3)	1000	125	62.5	1000		1000	
Water viscosity (m^2/s)	10^{-6}	4.42×10^{-8}	1.56×10^{-8}	4.42×10^{-8}	1.56×10^{-8}	10^{-6}	
Air density (kg/m^3)	1	0.125	0.0625	1		1	
Air viscosity (m^2/s)	1.48×10^{-5}	6.54×10^{-7}	2.31×10^{-7}	6.54×10^{-7}	2.31×10^{-7}	1.48×10^{-5}	
Surface tension (N/m)	0.07	1.37×10^{-4}	1.70×10^{-5}	1.09×10^{-3}	2.73×10^{-4}	0.07	
Inlet turbulent kinetic energy (m^2/s^2)	4.71×10^{-4}	5.89×10^{-5}	2.94×10^{-5}	5.89×10^{-5}	2.94×10^{-5}	5.89×10^{-5}	2.94×10^{-5}
Inlet energy dissipation rate ϵ_{in} (m^2/s^3)	1.05×10^{-3}	3.71×10^{-4}	2.63×10^{-4}	3.71×10^{-4}	2.63×10^{-4}	3.71×10^{-4}	2.63×10^{-4}

(iii) Results

Fig. 6 shows the time-averaged γ along the section A-A' for domains P1, P8, $P8_{PFr}$ and $P8_{TFr}$. The prototype shows a distribution of the time-averaged void fraction that is consistent with the description of high Re plunging jets provided by [47]. In particular, the flow shows the characteristic conical shape of the air-entrainment layer and the dispersion of bubbles due to the buoyancy effects outside the cone. The consequence of air entrainment in the flow is a rise of the free surface with respect to the initial conditions (Fig. 6a,b,c). Domains P8 and $P8_{PFr}$ have the identical shape of the air-entrainment layer showing also that the free surface reaches the same level, while $P8_{TFr}$ shows clear differences.

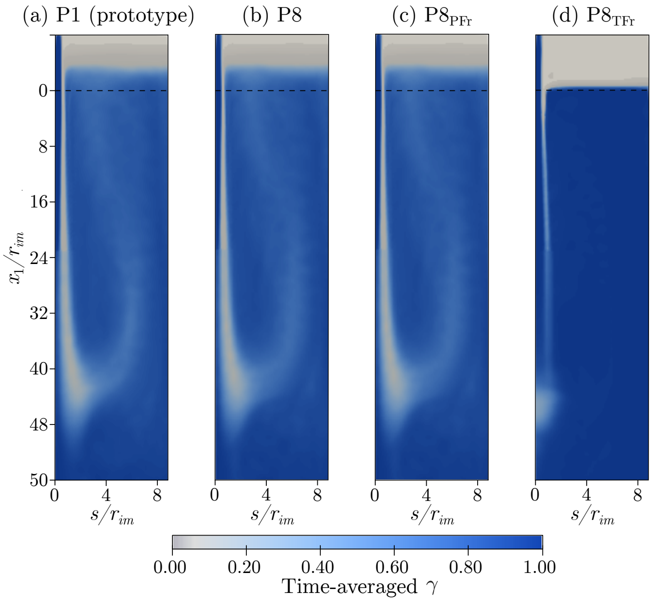

Figure 6. Time-averaged γ along the section A-A' for domains (a) P1, (b) P8, (c) $P8_{PFr}$ and (d) $P8_{TFr}$.

The following results are all shown along section A-A' at $\frac{x_1 - l_1}{r_{im}} = 1.60$. The distribution of the void fraction is compared with the experimental results of [13] in Fig. 7. The computed distribution and that measured in [13] are shown to have a close agreement. The novel scaling laws and precise Froude scaling reproduce the distribution of the void fraction of the prototype correctly, both in terms of the shape and magnitude. On the other hand, the traditional Froude scaling fails to describe the void fraction distribution.

Fig. 8 shows the time-averaged dimensionless velocity magnitude $\overline{U'}$ where for this case $U' = U/U_{im}$. In the prototype, the maximum value of $\overline{U'}$ is at the jet centreline and $\overline{U'}$ follows qualitatively the same velocity distribution as found in [49]. While the results of the domains P1, P8, P16, P8$_{\mathrm{PFr}}$ and P16$_{\mathrm{PFr}}$ are identical, $\overline{U'}$ for the domains P8$_{\mathrm{TFr}}$ and P16$_{\mathrm{TFr}}$ are lower than in the prototype.

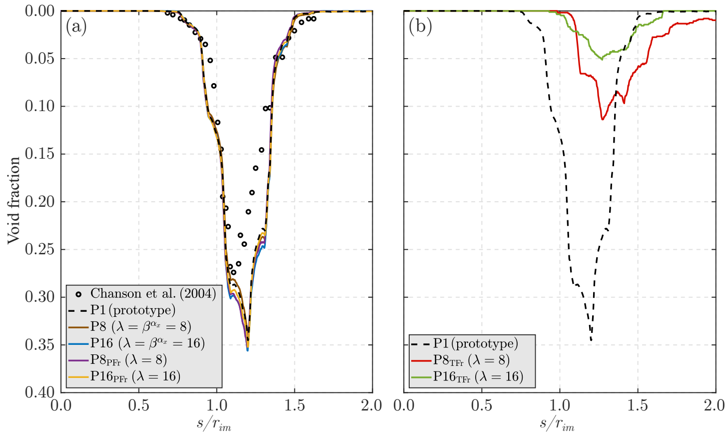

Figure 7. Distributions of the void fraction for the plunging jet for domains (a) P1, P8, P16, P8$_{\mathrm{PFr}}$ and P16$_{\mathrm{PFr}}$ and (b) P1, P8$_{\mathrm{TFr}}$ and P16$_{\mathrm{TFr}}$ along section A-A' at $\frac{x_1 - l_1}{r_{im}} = 1.60$.

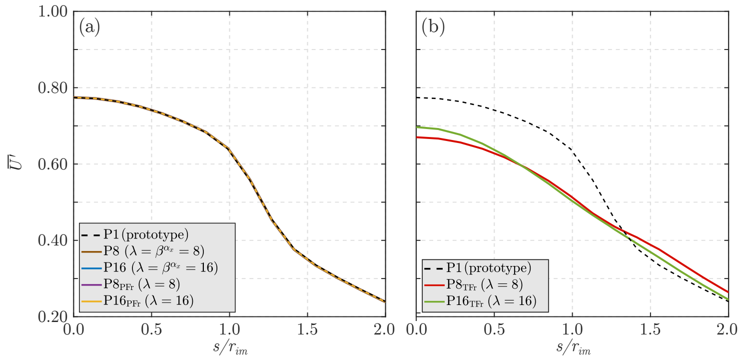

Figure 8. Time-averaged U' for the plunging jet for domains (a) P1, P8, P16, P8$_{\mathrm{PFr}}$ and P16$_{\mathrm{PFr}}$ and (b) P1, P8$_{\mathrm{TFr}}$ and P16$_{\mathrm{TFr}}$ along section A-A' at $\frac{x_1 - l_1}{r_{im}} = 1.60$.

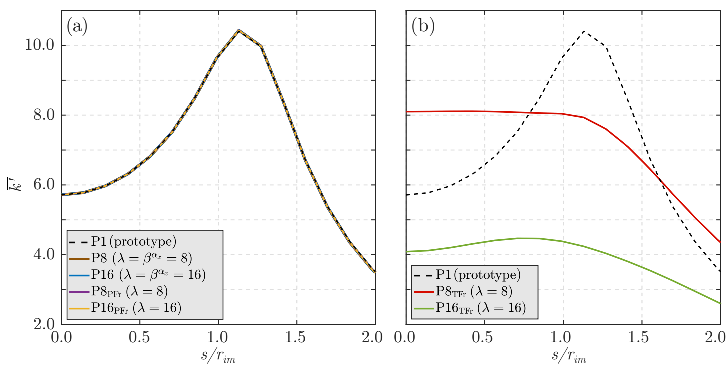

Figure 9. Time-averaged k' for the plunging jet for domains (a) P1, P8, P16, P8$_{\mathrm{PFr}}$ and P16$_{\mathrm{PFr}}$ and (b) P1, P8$_{\mathrm{TFr}}$ and P16$_{\mathrm{TFr}}$ along section A-A' at $\frac{x_1 - l_1}{r_{im}} = 1.60$.

Fig. 9 shows the time-averaged dimensionless turbulent kinetic energy $\overline{k'}$, where $k' = k/(g r_{im})$. In the prototype and self-similar domains the maximum value is $\overline{k'} = 10$ at $s/r_{im} = 1.0$ beyond which $\overline{k'}$ decreases to less than 4.0 at $s/r_{im} = 2.0$. On the other hand, the behaviour in the domains based on traditional Froude scaling is different. Indeed, $\overline{k'}$ in P8$_{\mathrm{TFr}}$ does not show a clear peak and remains almost constant as far as $s/r_{im} = 1.0$ beyond which it decreases. Moreover, the value of $\overline{k'}$ around the jet is higher in P8$_{\mathrm{TFr}}$ than in the prototype. However, P16$_{\mathrm{TFr}}$ shows a lower $\overline{k'}$ than the prototype with a maximum value of $\overline{k'} \approx 4.5$.

5. Discussion

Self-similarity has been achieved for the governing equations of air-water flows including surface tension expanding the scaling conditions reported in [28,29]. An advantage of this approach is that the scaling conditions are directly derived from the governing equations. This leads to more universal scaling laws than the Froude scaling laws [50]. Further, the choice of the scaling exponents α_x, α_t and α_ρ in the second column of Table 1 are user-defined (flexible). This implies that novel scaling laws can also be written in terms of a set of other variables to find different configurations. For example, it is shown that precise Froude scaling is obtained as a special case of the novel scaling laws. The CFD simulations conducted herein demonstrated that both the novel scaling laws and precise Froude scaling result in self-similar air-water flows, which would also be the case for another set of variables.

In the dam break flow, a significant deformation of the free surface is shown in the prototype after the flow impacts the obstacle, with a characteristic water tongue projected downstream of the obstacle. This behaviour is captured in all the domains scaled with the novel scaling laws; Figs. 3 show that k' is the same by using the novel scaling laws and k is thus self-similar. The phase fraction is also self-similar. This is a strong indication that surface tension effects are self-similar as well (Fig. 4) and it is also true for the domains D8$_{\mathrm{PFr}}$ and D16$_{\mathrm{PFr}}$, since precise Froude scaling is a special case of the novel scaling laws. On the other hand, the commonly applied traditional Froude scaling, relying on the same fluids as in the prototype, fails to reproduce the behaviour of the prototype. Indeed, Fig. 2f,g shows that the water tongue is not well predicted. After $t' = 2.7$, it collapses and the flow is reflected at the downstream wall. Scale effects are observed in k' and γ at point RW. Further, the flow reaches point RW later than in the prototype with increasing λ. Scale effects are also observed after the flow is re-reflected, particularly at the second peak of k'.

For the plunging jet, air entrainment plays a central role. Figs. 8a and 9a demonstrate that the novel scaling laws result in self-similarity for $\overline{U'}$ and $\overline{k'}$, i.e. these results collapse for P1, P8, P16, P8$_{\mathrm{PFr}}$ and P16$_{\mathrm{PFr}}$, while this is not the case for P8$_{\mathrm{TFr}}$ and P16$_{\mathrm{TFr}}$. The self-similarity of the distribution of the void fraction depends on density, viscous and surface tension effects. The prototype simulation captures the mechanism of air entrainment by a plunging jet (Fig. 5) including the formation of an air cavity between the impinging jet and the surrounding fluid, which collapses and reforms intermittently, entraining air bubbles that are transported by the flow. At this stage, air bubbles are advected in a turbulent shear flow and they are broken into smaller bubbles creating a conical air-entrainment layer. Subsequently, buoyancy determines the re-surfacing of bubbles in the portion of the flow outside the air layer [7,8,12]. This complex mechanism causes the air-entrainment layer in Fig. 6, where the novel scaling laws guarantee self-similarity. This is also true for the void fraction in Fig. 7 that is a consequence of the mechanism described above. On the other hand, Fig. 7b demonstrates that traditional Froude scaling fails to reproduce the void fraction distribution. By using ordinary water, the surface tension and viscosity are over-represented, therefore, the distribution of the void fraction gradually decreases with increasing λ. As expected, for increasing λ the flow regime changes, transitioning from high $\mathrm{Re} = 50840$ in the prototype to $\mathrm{Re} = 800$ in P16$_{\mathrm{TFr}}$, calculated by using U_{im}, r_{im} and ν_w. The modelling of this laminar flow with the k-ϵ turbulence model introduces also model, in addition to scale effects [2,3,47], which explain the results in Figs. 8b and 9b.

The need of the novel scaling laws for scaling fluid properties requires the modification or replacement of ordinary water in laboratory experiments, e.g., for values of λ comparable with the highest used here, i.e. $\lambda = 16$, where $\rho_w = 62.5$ kg/m^3, $\nu_w = 1.56 \times 10^{-8}$ m^2/s and $\sigma = 1.70 \times 10^{-5}$ N/m (Tables 3 and 5). There are options to alter the relevant fluid properties; the surface tension can be modified by adding ethanol to water [11] and the viscosity can also be reduced, e.g. [51] modelled a hydraulic jump with air. A more recent approach to change the water properties is based on nanofluids, i.e. nanoparticles are added to water [52,53]. A key advantage of the novel scaling laws is that fluids of different density than water, e.g. ethanol, now also qualify as potential candidates for laboratory experiments.

6. Conclusions

The Froude scaling laws are applied to model water flows at reduced size for almost one century. A significant disadvantage of Froude scaling is the potential for scale effects. This article shows how such scale effects in air-water flows are avoided with novel scaling laws based upon self-similarity of the governing equations. Lie group transformations are applied to the Reynolds-averaged Navier-Stokes equations where surface tension effects are included as a source term. This allows the modelling of hydrodynamic phenomena at small scale without viscous and surface tension scale effects. These novel scaling laws are more universal and flexible than the precise Froude scaling laws because different scaling configurations can be obtained, e.g. by scaling also the density of the fluid. In this study, the gravitational acceleration is kept constant and the scaling exponents of the variables are expressed as a function of the scaling exponents of the length α_x, time α_t and gravitational acceleration $\alpha_g = 0$.

The derived novel scaling laws were validated with the simulations of two air-water flow phenomena: (i) a dam break flow interacting with an obstacle and (ii) a plunging water jet. The numerical simulations demonstrated that the processes are correctly scaled, and showed perfect agreement at different scales for air entrainment and kinematic properties. The results of the precise Froude scaling, where the properties of the fluids are strictly scaled, demonstrate that a particular configuration of the novel scaling laws is also able to result in self-similarity. In contrast, the simulations based on traditional Froude scaling using ordinary water and air, as common in laboratory studies, show significant scale effects as expected.

Whilst this study provides a thorough numerical validation of the proposed scaling laws, future work aims to identify suitable fluids satisfying the novel scaling laws, which would enable the scaling of air-water flows without scale effects for the first time in an laboratory environment.

Acknowledgements. The authors would like to thank Dr David Hargreaves for helpful suggestions. The work was carried out as part of Daniele Catucci's PhD study, funded by the University of Nottingham Pro-Vice Chancellor Research Excellence Scholarship. The simulations were conducted on the University of Nottingham HPC clusters Augusta.

Appendix A - Derivation of the novel scaling laws

The remaining scaling conditions in Table 1, in addition to the ones presented in Sec. 2b, are derived here. The Lie group transformations for Eq. (2.2) yield the following equations in the transformed domain:

$$\beta^{\alpha_{U_\mathrm{i}}-\alpha_t}\frac{\partial U_\mathrm{i}^*}{\partial t^*}+\beta^{\alpha_{U_\mathrm{j}}+\alpha_{U_\mathrm{i}}-\alpha_{x_\mathrm{j}}}U_\mathrm{j}^*\frac{\partial U_\mathrm{i}^*}{\partial x_\mathrm{j}^*}=\beta^{\alpha_{U_\mathrm{i}}+\alpha_\nu-2\alpha_{x_\mathrm{j}}}\frac{\partial}{\partial x_\mathrm{j}^*}\left(\nu^*\frac{\partial U_\mathrm{i}^*}{\partial x_\mathrm{j}^*}\right)-\beta^{\alpha_{\overline{u_\mathrm{i}u_\mathrm{j}}}-\alpha_{x_\mathrm{j}}}\frac{\partial\overline{u_\mathrm{i}^*u_\mathrm{j}^*}}{\partial x_\mathrm{j}^*} \tag{6.1}$$
$$-\beta^{\alpha_p-\alpha_\rho-\alpha_{x_\mathrm{i}}}\frac{1}{\rho^*}\frac{\partial p^*}{\partial x_\mathrm{i}^*}+\beta^{\alpha_g}g_\mathrm{i}^*+\beta^{\alpha_{f_\sigma}-\alpha_\rho}\frac{f_\sigma^*}{\rho}.$$

Self-similarity is guaranteed if the scaling ratios of all terms in Eq. (6.1) are the same, implying that the exponents of all terms must be the same:

$$\begin{aligned}
\alpha_{U_1} - \alpha_t &= \alpha_{U_1} + \alpha_{U_1} - \alpha_{x_1} = \alpha_{U_2} + \alpha_{U_1} - \alpha_{x_2} = \alpha_{U_3} + \alpha_{U_1} - \alpha_{x_3} \\
&= \alpha_{U_1} + \alpha_\nu - 2\alpha_{x_1} = \alpha_{U_1} + \alpha_\nu - 2\alpha_{x_2} = \alpha_{U_1} + \alpha_\nu - 2\alpha_{x_3} \\
&= \alpha_{\overline{u_1 u_1}} - \alpha_{x_1} = \alpha_{\overline{u_1 u_2}} - \alpha_{x_2} = \alpha_{\overline{u_1 u_3}} - \alpha_{x_3} \\
&= \alpha_p - \alpha_\rho - \alpha_{x_1} \\
&= \alpha_g \\
&= \alpha_{f_\sigma} - \alpha_\rho.
\end{aligned} \tag{6.2}$$

$$\begin{aligned}
\alpha_{U_2} - \alpha_t &= \alpha_{U_1} + \alpha_{U_2} - \alpha_{x_1} = \alpha_{U_2} + \alpha_{U_2} - \alpha_{x_2} = \alpha_{U_3} + \alpha_{U_2} - \alpha_{x_3} \\
&= \alpha_{U_2} + \alpha_\nu - 2\alpha_{x_1} = \alpha_{U_2} + \alpha_\nu - 2\alpha_{x_2} = \alpha_{U_2} + \alpha_\nu - 2\alpha_{x_3} \\
&= \alpha_{\overline{u_2 u_1}} - \alpha_{x_1} = \alpha_{\overline{u_2 u_2}} - \alpha_{x_2} = \alpha_{\overline{u_2 u_3}} - \alpha_{x_3} \\
&= \alpha_p - \alpha_\rho - \alpha_{x_2} \\
&= \alpha_g \\
&= \alpha_{f_\sigma} - \alpha_\rho.
\end{aligned} \tag{6.3}$$

$$\begin{aligned}
\alpha_{U_3} - \alpha_t &= \alpha_{U_1} + \alpha_{U_3} - \alpha_{x_1} = \alpha_{U_2} + \alpha_{U_3} - \alpha_{x_2} = \alpha_{U_3} + \alpha_{U_3} - \alpha_{x_3} \\
&= \alpha_{U_3} + \alpha_\nu - 2\alpha_{x_1} = \alpha_{U_3} + \alpha_\nu - 2\alpha_{x_2} = \alpha_{U_3} + \alpha_\nu - 2\alpha_{x_3} \\
&= \alpha_{\overline{u_3 u_1}} - \alpha_{x_1} = \alpha_{\overline{u_3 u_2}} - \alpha_{x_2} = \alpha_{\overline{u_3 u_3}} - \alpha_{x_3} \\
&= \alpha_p - \alpha_\rho - \alpha_{x_3} \\
&= \alpha_g \\
&= \alpha_{f_\sigma} - \alpha_\rho.
\end{aligned} \tag{6.4}$$

The Lie group transformations for Eq. (2.3) result in

$$\beta^{\alpha_{f_\sigma}} f_\sigma^* = \beta^{\alpha_\sigma + \alpha_\kappa + \alpha_\gamma - \alpha_{x_\mathrm{i}}} \sigma^* \kappa^* \frac{\partial \gamma^*}{\partial x_\mathrm{i}^*}. \tag{6.5}$$

The dimension κ is the inverse of a length such that $\alpha_\kappa = -\alpha_{x_\mathrm{i}}$. Further, $\alpha_\gamma = 0$ because γ is dimensionless. Hence, Eq. (6.5) reduces to

$$\alpha_{f_\sigma} = \alpha_\sigma - 2\alpha_{x_\mathrm{i}}. \tag{6.6}$$

From Eqs. (6.2) to (6.4) the scaling exponents of the length dimensions along the i^{th} axis are obtained as

$$\alpha_{U_1} - \alpha_t = \alpha_{U_1} + \alpha_\nu - 2\alpha_{x_1} \quad \Rightarrow \quad \alpha_{x_1} = \frac{\alpha_t + \alpha_\nu}{2}, \tag{6.7}$$

$$\alpha_{U_2} - \alpha_t = \alpha_{U_2} + \alpha_\nu - 2\alpha_{x_2} \quad \Rightarrow \quad \alpha_{x_2} = \frac{\alpha_t + \alpha_\nu}{2}, \tag{6.8}$$

$$\alpha_{U_3} - \alpha_t = \alpha_{U_3} + \alpha_\nu - 2\alpha_{x_3} \quad \Rightarrow \quad \alpha_{x_3} = \frac{\alpha_t + \alpha_\nu}{2}. \tag{6.9}$$

In other words, the scaling exponents of the length scale must be identical for $\mathrm{i} = 1, 2, 3$ because the fluids are considered isotropic, therefore

$$\alpha_{x_1} = \alpha_{x_2} = \alpha_{x_3} = \alpha_x. \tag{6.10}$$

Similarly, α_{U_1}, α_{U_2} and α_{U_3} are obtained from Eqs. (6.2) to (6.4) as follows:

$$\alpha_{U_1} - \alpha_t = \alpha_{U_1} + \alpha_{U_1} - \alpha_x \quad \Rightarrow \quad \alpha_{U_1} = \alpha_x - \alpha_t, \tag{6.11}$$

$$\alpha_{U_2} - \alpha_t = \alpha_{U_2} + \alpha_{U_2} - \alpha_x \quad \Rightarrow \quad \alpha_{U_2} = \alpha_x - \alpha_t, \tag{6.12}$$

$$\alpha_{U_3} - \alpha_t = \alpha_{U_3} + \alpha_{U_3} - \alpha_x \quad \Rightarrow \quad \alpha_{U_3} = \alpha_x - \alpha_t. \tag{6.13}$$

Hence, α_{U_1}, α_{U_2} and α_{U_3} are also equal;

$$\alpha_{U_1} = \alpha_{U_2} = \alpha_{U_3} = \alpha_U = \alpha_x - \alpha_t. \tag{6.14}$$

Consequently, u_1, u_2 and u_3 have the same exponents in all directions as well because they are transformed by using the velocity ratio

$$\alpha_{u_1} = \alpha_{u_2} = \alpha_{u_3} = \alpha_u. \tag{6.15}$$

The results in Eqs. (6.10) to (6.15) are important because the selections of unique scaling exponents for length and velocity scales in the i$^{\text{th}}$ axis is necessary to achieve self-similarity of air-water flows. α_g, α_p and α_ν are obtained from Eqs. (6.2) to (6.4) and they can be written in terms of α_x, α_t and α_ρ as

$$\alpha_U - \alpha_t = \alpha_g \quad \Rightarrow \quad \alpha_g = \alpha_x - 2\alpha_t, \tag{6.16}$$

$$\alpha_U - \alpha_t = \alpha_p - \alpha_\rho - \alpha_x \quad \Rightarrow \quad \alpha_p = 2\alpha_x - 2\alpha_t + \alpha_\rho, \tag{6.17}$$

$$\alpha_U - \alpha_t = \alpha_U + \alpha_\nu - 2\alpha_x \quad \Rightarrow \quad \alpha_\nu = 2\alpha_x - \alpha_t. \tag{6.18}$$

By using Eqs. (6.2) and (6.6)

$$\alpha_U - \alpha_t = \alpha_{f_\sigma} - \alpha_\rho \quad \Rightarrow \quad \alpha_x - 2\alpha_t = \alpha_\sigma - 2\alpha_x - \alpha_\rho, \tag{6.19}$$

from which

$$\alpha_\sigma = 3\alpha_x - 2\alpha_t + \alpha_\rho. \tag{6.20}$$

Similarly, Eqs. (2.4) to (2.7) are transformed by keeping $C_{\epsilon 1}$, $C_{\epsilon 2}$, C_μ, C_{σ_k} and C_{σ_ϵ} as dimensionless coefficients

$$-\beta^{\alpha_{\overline{uu}}}\overline{u_{\mathrm{i}}^* u_{\mathrm{j}}^*} = \beta^{\alpha_{\nu_t}+\alpha_U-\alpha_x}\nu_t^*\frac{\partial U_{\mathrm{i}}^*}{\partial x_{\mathrm{j}}^*} + \beta^{\alpha_{\nu_t}+\alpha_U-\alpha_x}\nu_t^*\frac{\partial U_{\mathrm{j}}^*}{\partial x_{\mathrm{i}}^*} - \frac{2}{3}\beta^{\alpha_k}k^*\delta_{\mathrm{ij}}, \tag{6.21}$$

$$\beta^{\alpha_{\nu_t}}\nu_t^* = \beta^{2\alpha_k-\alpha_\epsilon}C_\mu\frac{k^{*2}}{\epsilon^*}, \tag{6.22}$$

$$\begin{aligned}\beta^{\alpha_k-\alpha_t}\frac{\partial k^*}{\partial t^*} + \beta^{\alpha_U+\alpha_k-\alpha_x}U_{\mathrm{j}}^*\frac{\partial k^*}{\partial x_{\mathrm{j}}^*} = \beta^{\alpha_{P_k}}P_k^* - \beta^{\alpha_\epsilon}\epsilon^* + \beta^{\alpha_\nu+\alpha_k-2\alpha_x}\frac{\partial}{\partial x_{\mathrm{j}}^*}\left(\nu^*\frac{\partial k^*}{\partial x_{\mathrm{j}}^*}\right) \\ +\beta^{\alpha_{\nu_t}+\alpha_k-2\alpha_x}\frac{\partial}{\partial x_{\mathrm{j}}^*}\left(\nu_t^*/C_{\sigma_k}\frac{\partial k^*}{\partial x_{\mathrm{j}}^*}\right)\end{aligned} \tag{6.23}$$

and

$$\beta^{\alpha_\epsilon-\alpha_t}\frac{\partial \epsilon^*}{\partial t^*}+\beta^{\alpha_U+\alpha_\epsilon-\alpha_x}U_{\mathrm{j}}^*\frac{\partial \epsilon^*}{\partial x_{\mathrm{j}}^*}=\beta^{\alpha_\epsilon+\alpha_{P_k}-\alpha_k}C_{\epsilon 1}\frac{\epsilon^*}{k^*}P_k^*-\beta^{2\alpha_\epsilon-\alpha_k}C_{\epsilon 2}\frac{\epsilon^{*2}}{k^*} \tag{6.24}$$
$$+\beta^{\alpha_\nu+\alpha_\epsilon-2\alpha_x}\frac{\partial \nu^*}{\partial x_{\mathrm{j}}^*}\left(\frac{\partial \epsilon^*}{\partial x_{\mathrm{j}}^*}\right)+\beta^{\alpha_{\nu_t}+\alpha_\epsilon-2\alpha_x}\frac{\partial}{\partial x_{\mathrm{j}}^*}\left[\left(\frac{\nu_t^*}{C_{\sigma_\epsilon}}\right)\frac{\partial \epsilon^*}{\partial x_{\mathrm{j}}^*}\right].$$

For Eqs. (6.21) to (6.24) to be self-similar, the following conditions must hold

$$\begin{aligned}\alpha_{\overline{uu}}&=\alpha_{\nu_t}+\alpha_U-\alpha_x\\&=\alpha_{\nu_t}+\alpha_U-\alpha_x\\&=\alpha_k,\end{aligned} \tag{6.25}$$

$$\alpha_{\nu_t}=2\alpha_k-\alpha_\epsilon, \tag{6.26}$$

$$\begin{aligned}\alpha_k-\alpha_t&=\alpha_U+\alpha_k-\alpha_x\\&=\alpha_{P_k}\\&=\alpha_\epsilon\\&=\alpha_\nu+\alpha_k-2\alpha_x\\&=\alpha_{\nu_t}+\alpha_k-2\alpha_x\end{aligned} \tag{6.27}$$

and

$$\begin{aligned}\alpha_\epsilon-\alpha_t&=\alpha_U+\alpha_\epsilon-\alpha_x\\&=\alpha_\epsilon+\alpha_{P_k}-\alpha_k\\&=2\alpha_\epsilon-\alpha_k\\&=\alpha_\nu+\alpha_\epsilon-2\alpha_x\\&=\alpha_{\nu_t}+\alpha_\epsilon-2\alpha_x.\end{aligned} \tag{6.28}$$

ν_t has the same dimension as ν, therefore, Eq. (6.18) yields

$$\alpha_{\nu_t}=2\alpha_x-\alpha_t. \tag{6.29}$$

$\alpha_{\overline{uu}}$ is the same in all directions and it is calculated from Eqs. (6.25) and (6.29) as

$$\alpha_{\overline{uu}}=\alpha_{\nu_t}+\alpha_U-\alpha_x \quad\Rightarrow\quad \alpha_{\overline{uu}}=2\alpha_x-2\alpha_t. \tag{6.30}$$

From Eq. (6.25) α_k is obtained ($\alpha_k=2\alpha_x-2\alpha_t$). Finally, α_ϵ and α_{P_k} are obtained from Eqs. (6.26) and (6.27) as

$$\alpha_\epsilon=2\alpha_k-\alpha_{\nu_t} \quad\Rightarrow\quad \alpha_\epsilon=2\alpha_x-3\alpha_t, \tag{6.31}$$
$$\alpha_{P_k}=\alpha_k-\alpha_t \quad\Rightarrow\quad \alpha_{P_k}=2\alpha_x-3\alpha_t. \tag{6.32}$$

The Lie group transformations are also applied to the initial and boundary conditions. The initial velocity $U(x_{\mathrm{i}},t=0)=U_{\mathrm{i}_0}(x_{\mathrm{i}})$ and pressure fields $p(x_{\mathrm{i}},t=0)=p_0(x_{\mathrm{i}})$ are transformed as

$$U_{\mathrm{i}_0}^*(x_\mathrm{i}^*) = \beta^{-\alpha_U} U_{\mathrm{i}_0}(x_\mathrm{i}) = \beta^{-\alpha_U} U_{\mathrm{i}_0}(\beta^{\alpha_x} x_\mathrm{i}^*), \tag{6.33}$$

$$p_0^*(x_\mathrm{i}^*) = \beta^{-\alpha_p} p_0(x_\mathrm{i}) = \beta^{-\alpha_p} p_0(\beta^{\alpha_x} x_\mathrm{i}^*). \tag{6.34}$$

Another boundary condition is the zero gradient $\frac{\partial}{\partial x_\mathrm{i}}\phi = 0$ for a flow variable ϕ. This gradient condition is transformed as $\beta^{\alpha_\phi - \alpha_x} \frac{\partial}{\partial x_\mathrm{i}}\phi^* = 0$. Since $\beta \neq 0$, this does not pose any limitation in the scaling conditions ($\frac{\partial}{\partial x_\mathrm{i}}\phi^* = 0$).

References

1. Hager WH, Castro-Orgaz O. 2017 William Froude and the Froude number. *Journal of Hydraulic Engineering* **143**, 02516005.
2. Heller V. 2011 Scale effects in physical hydraulic engineering models. *Journal of Hydraulic Research* **49(3)**, 293–306.
3. Hughes SA. 1993 *Physical models and laboratory techniques in coastal engineering* vol. 7. Singapore: World Scientific.
4. Ali SZ, Dey S. 2017 Origin of the scaling laws of sediment transport. *Proceedings of the Royal Society A: Mathematical, Physical and Engineering Sciences* **473**, 20160785.
5. Frisch U. 1995 *Turbulence: the legacy of AN Kolmogorov*. Cambridge: Cambridge University Press.
6. Heller V. 2017 Self-similarity and Reynolds number invariance in Froude modelling. *Journal of Hydraulic Research* **55(3)**, 293–309.
7. Biń AK. 1993 Gas entrainment by plunging liquid jets. *Chemical Engineering Science* **48(21)**, 3585–3630.
8. Kiger KT, Duncan JH. 2012 Air-entrainment mechanisms in plunging jets and breaking waves. *Annual Review of Fluid Mechanics* **44**, 563–596.
9. Felder S, Chanson H. 2017 Scale effects in microscopic air-water flow properties in high-velocity free-surface flows. *Experimental Thermal and Fluid Science* **83**, 19–36.
10. Heller V, Hager WH, Minor H-E. 2008 Scale effects in subaerial landslide generated impulse waves. *Experiments in Fluids* **44(5)**, 691–703.
11. Stagonas D, Warbrick D, Muller G, Magagna D. 2011 Surface tension effects on energy dissipation by small scale, experimental breaking waves. *Coastal Engineering* **58(9)**, 826–836.
12. Blenkinsopp C, Chaplin J. 2007 Void fraction measurements in breaking waves. *Proceedings of the Royal Society A: Mathematical, Physical and Engineering Sciences* **463**, 3151–3170.
13. Chanson H, Aoki S, Hoque A. 2004 Physical modelling and similitude of air bubble entrainment at vertical circular plunging jets. *Chemical Engineering Science* **59(4)**, 747–758.
14. Wang H, Chanson H. 2015 Air entrainment and turbulent fluctuations in hydraulic jumps. *Urban Water Journal* **12(6)**, 502–518.
15. Leighton TG, Coles DG, Srokosz M, White PR, Woolf DK. 2018 Asymmetric transfer of CO2 across a broken sea surface. *Scientific Reports* **8**, 1–9.
16. Mustaffa NIH, Ribas-Ribas M, Banko-Kubis HM, Wurl O. 2020 Global reduction of in situ CO2 transfer velocity by natural surfactants in the sea-surface microlayer. *Proceedings of the Royal Society A: Mathematical, Physical and Engineering Sciences* **476**, 20190763.
17. Barenblatt GI. 1996 *Scaling, self-similarity, and intermediate asymptotics: dimensional analysis and intermediate asymptotics*. Cambridge: Cambridge University Press.
18. Barenblatt GI. 2003 *Scaling (Vol. 34)*. Cambridge: Cambridge University Press.
19. Henriksen RN. 2015 *Scale invariance: self-similarity of the physical world*. Weinheim, Germany: John Wiley & Sons.
20. Zohuri B. 2015 *Dimensional analysis and self-similarity methods for engineers and scientists*. Cham: Springer.
21. Polyanin AD, Manzhirov AV. 2008 *Handbook of integral equations*. London: Chapman and Hall.
22. Lie S. 1880 Theorie der Transformationsgruppen I. *Mathematische Annalen* **16(4)**, 441–528.
23. Bluman GW, Cole JD. 1974 *Similarity methods for differential equations* vol. 13. New York: Springer.
24. Bluman G, Anco S. 2002 *Symmetry and integration methods for differential equations* vol. 154. New York: Springer.

25. Haltas I, Kavvas M. 2011 Scale invariance and self-similarity in hydrologic processes in space and time. *Journal of Hydrologic Engineering* **16(1)**, 51–63.
26. Polsinelli J, Kavvas ML. 2016 A comparison of the modern Lie scaling method to classical scaling techniques. *Hydrology and Earth System Sciences* **20**, 2669–2678.
27. Ercan A, Kavvas ML, Haltas I. 2014 Scaling and self-similarity in one-dimensional unsteady open channel flow. *Hydrological Processes* **28**, 2721–2737.
28. Ercan A, Kavvas ML. 2015 Scaling and self-similarity in two-dimensional hydrodynamics. *Chaos: An Interdisciplinary Journal of Nonlinear Science* **25(7)**, 075404.
29. Ercan A, Kavvas ML. 2017 Scaling relations and self-similarity of 3-dimensional Reynolds-averaged Navier-Stokes equations. *Scientific Reports* **7(1)**, 6416.
30. Huang W, Yang Q, Xiao H. 2009 CFD modeling of scale effects on turbulence flow and scour around bridge piers. *Computers & Fluids* **38**, 1050–1058.
31. Oliveira FS, Contente J. 2013 Scale effects in numerical modelling of beach profile erosion. *Journal of Coastal Research* **65**, 1815–1820.
32. Torres C, Borman D, Sleigh A, Neeve D. 2018 Investigating scale effects of a hydraulic physical model with 3D CFD. In *Smart Dams and Reservoirs-Proceedings of the 20th Biennial Conference of the British Dam Society* pp. 89–101. ICE.
33. Carr K, Ercan A, Kavvas M. 2015 Scaling and self-similarity of one-dimensional unsteady suspended sediment transport with emphasis on unscaled sediment material properties. *Journal of Hydraulic Engineering* **141**, 04015003.
34. Zhainakov AZ, Kurbanaliev A. 2013 Verification of the open package OpenFOAM on dam break problems. *Thermophysics and Aeromechanics* **20(4)**, 451–461.
35. Greenshields CJ. 2019 *The Open Source CFD Toolbox, User Guide*. OpenFOAM Foundation Ltd.
36. Pope SB. 2000 *Turbulent Flows*. Cambridge: Cambridge University Press.
37. Launder B, Spalding D. 1974 The numerical computation of turbulent flows. *Computer Methods in Applied Mechanics and Engineering* **3**, 269–289.
38. Fan W, Anglart H. 2020 varRhoTurbVOF: A new set of volume of fluid solvers for turbulent isothermal multiphase flows in OpenFOAM. *Computer Physics Communications* **247**, 106876.
39. Ercan A, Kavvas ML. 2015 Self-similarity in incompressible Navier-Stokes equations. *Chaos: An Interdisciplinary Journal of Nonlinear Science* **25(12)**, 123126.
40. Brackbill JU, Kothe DB, Zemach C. 1992 A continuum method for modeling surface tension. *Journal of Computational Physics* **100(2)**, 335–354.
41. Deshpande SS, Anumolu L, Trujillo MF. 2012 Evaluating the performance of the two-phase flow solver interFoam. *Computational Science & Discovery* **5(1)**, 014016.
42. Roenby J, Bredmose H, Jasak H. 2016 A computational method for sharp interface advection. *Royal Society Open Science* **3**, 160405.
43. Issakhov A, Zhandaulet Y, Nogaeva A. 2018 Numerical simulation of dam break flow for various forms of the obstacle by VOF method. *International Journal of Multiphase Flow* **109**, 191–206.
44. Kleefsman K, Fekken G, Veldman A, Iwanowski B, Buchner B. 2005 A volume-of-fluid based simulation method for wave impact problems. *Journal of Computational Physics* **206(1)**, 363–393.
45. Courant R, Friedrichs K, Lewy H. 1967 On the partial difference equations of mathematical physics. *IBM Journal of Research and Development* **11**, 215–234.
46. Boualouache A, Zidouni F, Mataoui A. 2018 Numerical visualization of plunging water jet using volume of fluid model. *Journal of Applied Fluid Mechanics* **11(1)**, 95–105.
47. Hassan SH, Guo T, Vlachos PP. 2019 Flow field evolution and entrainment in a free surface plunging jet. *Physical Review Fluids* **4**, 104603.
48. Massey Jr FJ. 1951 The Kolmogorov-Smirnov test for goodness of fit. *Journal of the American Statistical Association* **46**, 68–78.
49. McKeogh E, Ervine D. 1981 Air entrainment rate and diffusion pattern of plunging liquid jets. *Chemical Engineering Science* **36**, 1161–1172.
50. Kline SJ. 1965 *Similitude and approximation theory*. London: McGraw-Hill.
51. Rouse H, Siao TT, Nagaratnam S. 1958 Turbulence characteristics of the hydraulic jump. *Journal of the Hydraulics Division* **84**, 1–30.
52. Lu G, Duan YY, Wang XD. 2014 Surface tension, viscosity, and rheology of water-based nanofluids: a microscopic interpretation on the molecular level. *Journal of Nanoparticle Research* **16(9)**, 2564.
53. Xu M, Liu H, Zhao H, Li W. 2013 How to decrease the viscosity of suspension with the second fluid and nanoparticles? *Scientific Reports* **3**, 3137.